Check for updates

Magnetic imaging using geometrically constrained nano-domain walls†

Héctor Corte-León, [ID] *[a] Luis Alfredo Rodríguez, [ID] [b] Matteo Pancaldi, [ID] [c] Christophe Gatel, [ID] [d] David Cox, [ID] [a] Etienne Snoeck, [ID] [d] Vladimir Antonov, [ID] [e] Paolo Vavassori [ID] [c,f] and Olga Kazakova [ID] [a]

Magnetic nanostructures, as part of hybrid CMOS technology, have the potential to overcome silicon's scaling limit. However, a major problem is how to characterize their magnetization without disturbing it. Magnetic force microscopy (MFM) offers a convenient way of studying magnetization, but spatial resolution and sensitivity are usually boosted at the cost of increasing probe-sample interaction. By using a single magnetic domain wall (DW), confined in a V-shape nanostructure fabricated at the probe apex, it is demonstrated here that the spatial resolution and the magnetic sensitivity can be decoupled and both enhanced. Indeed, owing to the nanostructure's strong shape anisotropy, DW-probes have 2 high and 2 low magnetic moment states with opposite polarities, characterised by a geometrically constrained pinned DW, and curled magnetization, respectively. Electron holography studies, supported by numerical simulations, and *in situ* MFM show that the DW-probe state can be controlled, and thus used as a switchable tool with a low/high stray field intensity.

Introduction

Magnetic force microscopy (MFM) enables imaging magnetization distribution with nanoscale resolution, down to ~10 nm,[1] which is a key requirement for studying novel magnetic nanostructures such as hybrid CMOS structures, *e.g.* magnetoresistive random-access memory devices,[2–4] or magnetic sensors used for Lab-On-a-Chip applications.[5,6] However, smaller and more complex nanostructures require not only higher resolution MFM, but also the ability to extract detailed and accurate information about the magnetization of the sample with minimal invasiveness. Thus, the main challenges that modern MFM technology is facing are (i) to increase the sensitivity (both magnetic sensitivity and spatial resolution)[7] and (ii) to minimize the mutual interference between the probe and sample magnetization.[8–11] The latter requirement translates naturally into the need to use low magnetic moment probes

with high coercivity. However, this automatically leads to a drastic reduction of magnetic sensitivity, which is presently achievable by employing a high magnetic moment probe.

Different solutions have been previously proposed to tackle the above challenges. For instance, sharp probes with thin magnetic coating provide better spatial resolution,[10,12–16] but at the price of a reduced magnetic moment, *i.e.* a lowered magnetic sensitivity. Thicker coatings, or hard magnetic materials, produce a larger magnetic moment[1,16–20] that improves the magnetic sensitivity and the probe's resilience to magnetic perturbations, but at the cost of a dramatic increase of its interaction with the sample's magnetization and a loss in resolution due to the increased physical radius of the probe's apex.

In general, when using a uniform magnetic coating, its thickness is linked to the sharpness of the probe's apex, as well as the stray field and coercivity of the probe. This does not allow for much freedom in the variation/optimization of the probe.[19] Thereby, the most common scenario is to use a probe matching sample properties in each particular case. However, this approach becomes impractical when the sample under study is magnetically heterogeneous, comprised of areas with high and low anisotropy and magnetization, or with magnetic domain walls (DWs) generating high gradient stray fields.[9] These scenarios are more and more frequent situations faced by modern cutting-edge nanotechnology,[21] arising from both the continuous reduction in size and the use of composite, multifunctional materials that are characterized by intrinsically large heterogeneity of properties. In such cases, the stray

[a]National Physical Laboratory, Teddington, TW11 0LW, UK.
E-mail: hector.corte@npl.co.uk
[b]Department of Physics, Universidad del Valle, A. A. 25360 Cali, Colombia
[c]CIC nanoGUNE, Donostia-San Sebastian, E-20018, Spain
[d]CEMES CNRS-UPR 8011, Université de Toulouse, 29 rue Jeanne Marvig, 31055 Toulouse, France
[e]Physics Department, Royal Holloway University of London, Egham, TW20 0EX, UK
[f]IKERBASQUE, Basque Foundation for Science, Bilbao E-48013, Spain
†Electronic supplementary information (ESI) available. See DOI: 10.1039/c8nr07729k

field generated by the probe may induce changes in the magnetization of low anisotropy regions,[22] while regions with high magnetization generate intense stray fields that may affect the magnetic moment of the probe if its anisotropy is not strong enough.[23] Both effects will severely reduce reliability of MFM measurements; hence it would be of the utmost relevance to develop probes with a sufficiently large coercivity, *i.e.* stability, and with a magnetic moment that can be controllably switched between high and low moment states on demand.

To achieve higher spatial resolution, probes modified with magnetic nanoparticles[15,24] or nanowires[8,25–30] were previously demonstrated. By using such magnetic nanostructures, it is possible to increase lateral resolution, but usually at the cost of a reduced magnetic signal and probe stability, given by the intrinsically small magnetic moment and anisotropy of the structure.

A different approach utilizes multilayered magnetic probes, designed to have an uncompensated magnetic moment at the probe's apex, which results in the simultaneous increase of probe's magnetic sensitivity and anisotropy.[31–33] However, this approach unavoidably results in a substantial increase of probe radius, with the consequent loss in spatial resolution.

Finally, other approaches involve modification of the MFM technique rather than the magnetic probes, *e.g.* imaging the same sample twice but with the probe magnetized in opposite directions;[34,35] driving the probe at different frequencies during topography and lift scans,[36,37] or using dual probes where one of the probes is non-magnetic and records the topography signal, while the second one (at higher distance from the surface), records the magnetic signal.[38] However, none of the solutions mentioned above fully addresses all the aforementioned challenges.

Here, we propose a novel approach to overcome these problems by implementing geometrically constrained nanosize DWs[39] directly onto MFM probes (DW-probe). This is achieved substituting the conventional uniform magnetic coating with a patterned V-shaped magnetic nanostructure on one side of the probe's pyramid (see Fig. 1). This DW-probe features several properties that makes it suitable for high-resolution imaging of heterogeneous samples. First, spatial and magnetic resolutions are decoupled, since the former one depends solely on the physical apex of the probe and the later one on the dimensions and position of the V-shaped structure, which does not coincide with the apex [see Fig. 1(d) and Fig. S1 and S2 in the ESI†]. Second, the V-shaped structure can be set into four different stable magnetization states [see Fig. 1(d) inset] by applying a magnetic field. Two of them are high moment magnetic states with a head-to-head or tail-to-tail (HH or TT, respectively) DWs that have opposite polarity (HH-DW with north polarity and TT-DW with south polarity) at the V-apex of the nanostructure.[40,41] The other two states at the V-apex are low moment "curl" magnetic states caused either by removal or annihilation of a DW. The presence of the disks at the end of the V-shaped nanostructure favors the nucleation of reversed magnetization, thus facilitating the nucleation and annihilation of DWs, *i.e.*, switching the magnetic moment of
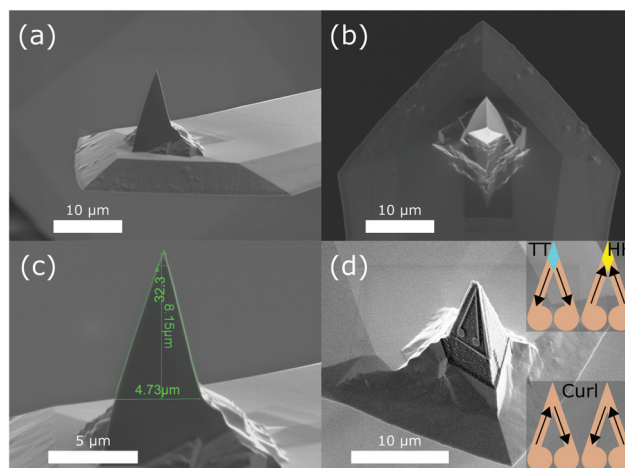

Fig. 1 SEM images of commercial and custom-made DW-probes. (a)–(c) Original commercial NANOSENSORS™ PPP-MFMR AFM probe. (d) DW-probe: V-shape nanostructure defined by FIB ion etching on one side of the probe apex. Inset: Schematics of 4 possible magnetization states with TT/HH DWs marked in turquoise/yellow colour, respectively.

the tip from low to high *via* the external magnetic field. At the same time, the geometrical constraint, provided by the V-shaped nanostructure, bestow an exceptional stability to the 4 states against local magnetic perturbations (*e.g.*, intense stray fields from the sample). Hence this probe has the potential to overcome the two main challenges stated above (*i.e.* increasing resolution and reduce probe-sample interaction), and become an effective solution for studies of nanoscale heterogeneous magnetic samples.

The results presented here include: a detailed study of the four states of the DW-probe by means of electron holography (EH) investigations[42] and numerical simulations; the remotely controllable switching of magnetization of the DW-probe demonstrated by *in situ* MFM imaging; and the comparison of the DW-probe with commercial low moment probes by imaging a particularly challenging magnetic nanostructure.

Results

Fig. 2 displays the results of EH experiments, where Fig. 2(a–c) show the electron beam phase shift (in radians) due to the stray field emanating from the DW-probe at different magnetization state of the probe, from TT to curl to HH respectively. Images in Fig. 2(d–f) show the magnetic flux line representations of the corresponding phase shift images in Fig. 2(a–c) (see details in the Experimental section). It can be seen that the TT and HH states generate a strong stray field emanating from the apex, which corresponds to a large monopole-like magnetic charge[39] localized at the outer corner of the V-shaped nanostructure (*i.e.* equivalent charge distributions schematically shown as 'north pole' in red for HH and 'south pole' in blue for TT configurations, with size of the circles indi-
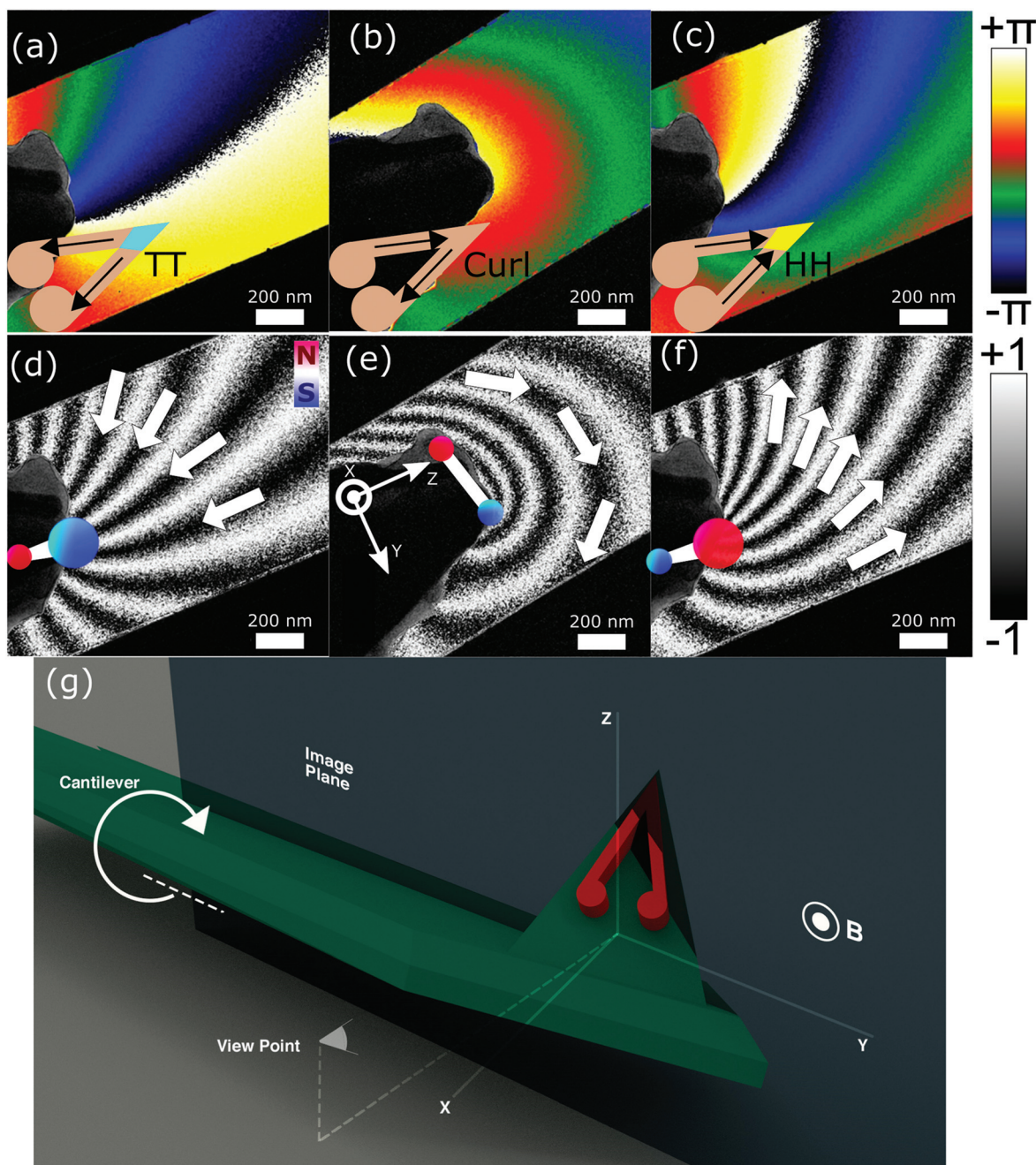
Fig. 2 DW-probe stray field imaged using EH: (a–c) phase and (d–f) magnetic flux images. (a) and (d) TT configuration. (b) and (e) curl state configuration. (c) and (f) HH state configuration. Schematics in (d–f) shows dipole approximation of the stray field, with arrows indicating field direction and size of the circles representing the relative strength of the magnetic poles. (g) Schematics of the relative orientation of the probe and the image plane: during imaging the probe's pyramid is oriented along $+z$-axis; in order to change the magnetization state of the probe the cantilever is aligned along the $-x$-axis parallel to the magnetic field. The coordinates in (e) and (g) are the same.

cating the dominating pole character). The curl state [Fig. 2(b) and (e)] creates field lines that close around the apex of the probe, which corresponds to a weak magnetic dipole-like charge aligned perpendicular to the V-structure bisector. The stray field images shown in Fig. 2 agree with the interpretation of the V-shaped nanostructure acting as a four-state device, where two states have a DW pinned at the apex of the probe

with strong emanating stray field and two states without DW and much weaker stray field.

This picture is further corroborated by the results of the OOMMF micromagnetic simulations of the V-shape in the DW-probes (Fig. 3). Results shown are at zero field after applying a saturating magnetic field either parallel/perpendicular to the V-shape bisector [top/bottom of Fig. 3(a), (b) and (c) for the
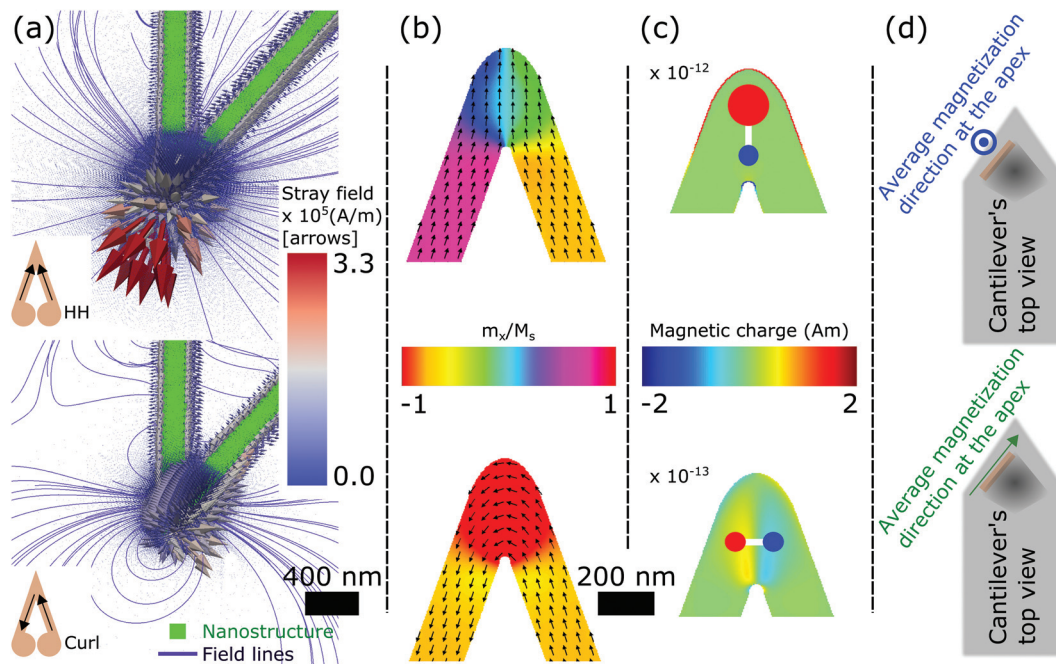
Fig. 3 DW-probe numerically simulated magnetization and stray field. (a) Stray field created by the V-shaped magnetic nanostructure when magnetization is either in HH state (top row) or curl state (bottom row). Corresponding images for (b) magnetization, (c) magnetic charge distribution and (d) the direction of the stray field during MFM imaging.

stray field, magnetization and magnetic charge density distribution, respectively]. The state on top of Fig. 3(a–c) corresponds to HH state, with a DW pinned at the corner of the nanostructure and a strong stray field where the spatial distribution is similar to the field shown in Fig. 2(f). In Fig. 3(c) the monopole-like charge distribution (surface magnetic charge in this case) has been drawn schematically as two circles of different sizes (*i.e.* red and blue), for the only purpose to illustrate the dominating magnetic pole type corresponding to the surface magnetic charge located at the outer edge of the V-structure (red contour in figure). The state shown at the bottom of Fig. 3(a–c) corresponds to the curl state, corresponding to a horizontal dipole-like charge distribution (volume magnetic charge in this case) that results in the field lines across the corner, similarly to Fig. 2(e). Thus, the OOMMF simulations displayed in Fig. 3 are in good agreement with the experimental EH results (Fig. 2).

We further compared the performance of the DW-probe (resonant frequency f_0 = 72.245 kHz, Q-factor = 205, and spring constant k = 3.63 N m^{-1}) with commercial probes with similar mechanical properties: a NANOSENSORS™ PPP-MFMR AFM probe[43] (f_0 = 67.346 kHz, Q = 201, and k = 4.00 N m^{-1}), and a low moment (LM) probe,[44] NT-MDT MFM_LM, with similar mechanical properties (f_0 = 65.033 kHz, Q = 195, and k = 2.46 N m^{-1}). The three probes were used to scan the same area of a floppy disk with a simple magnetization pattern composed of bits of data with in-plane magnetization and sufficiently high coercivity (*i.e.* suitable to be imaged under applied magnetic fields without perturbing its magnetization),

see Fig. 4(a). The magnetic imaging was performed in the two-pass standard MFM scan with a lift height of 40 nm, and the oscillation amplitude of the probes was adjusted to be the same (14 nm). The three probes were exposed to the north pole of a permanent magnet prior to the scan. Bottom graph in Fig. 4(a), which corresponds to cross sections taken from the top images in Fig. 4(a), demonstrates that the commercial NANOSENSOR™ PPP-MFMR AFM probe shows the greatest phase contrast (~2.25°), whilst the low moment NT-MDT MFM_LM probe has the smallest contrast difference (~0.25°). The DW-probe in TT state (*i.e.* after exposing the probe to the north pole of a magnet), has an intermediate contrast (~0.5°). This demonstrates that, despite having much less magnetic material than the non-modified probe, the localization of the magnetic moment at the probe apex, enabled by the pinning geometrical confinement of a DW at the corner of the V-shaped nanostructure, results in a sizeable interaction between probe and sample magnetization, two times larger than the one occurring with a low moment probe.

Fig. 4(b) and (c) show the same floppy disk scanned with the DW-probe, while an out-of-plane magnetic field of varying intensity is being applied. In Fig. 4(b) line profiles along directions marked by blue and red dotted lines are shown.

In Fig. 4(b), first, at y = 0 µm, a positive magnetic field of 70 mT is applied (*i.e.* a TT state is induced in the V-shaped nanostructure). At the beginning of the scan, 0 < y < 20 µm, the field is reduced step-wise to 40, 0, −40, and −70 mT. The image and profiles in Fig. 4(b) demonstrate that for B = −40 mT (15 µm < y < 20 µm) the signal amplitude is reduced,
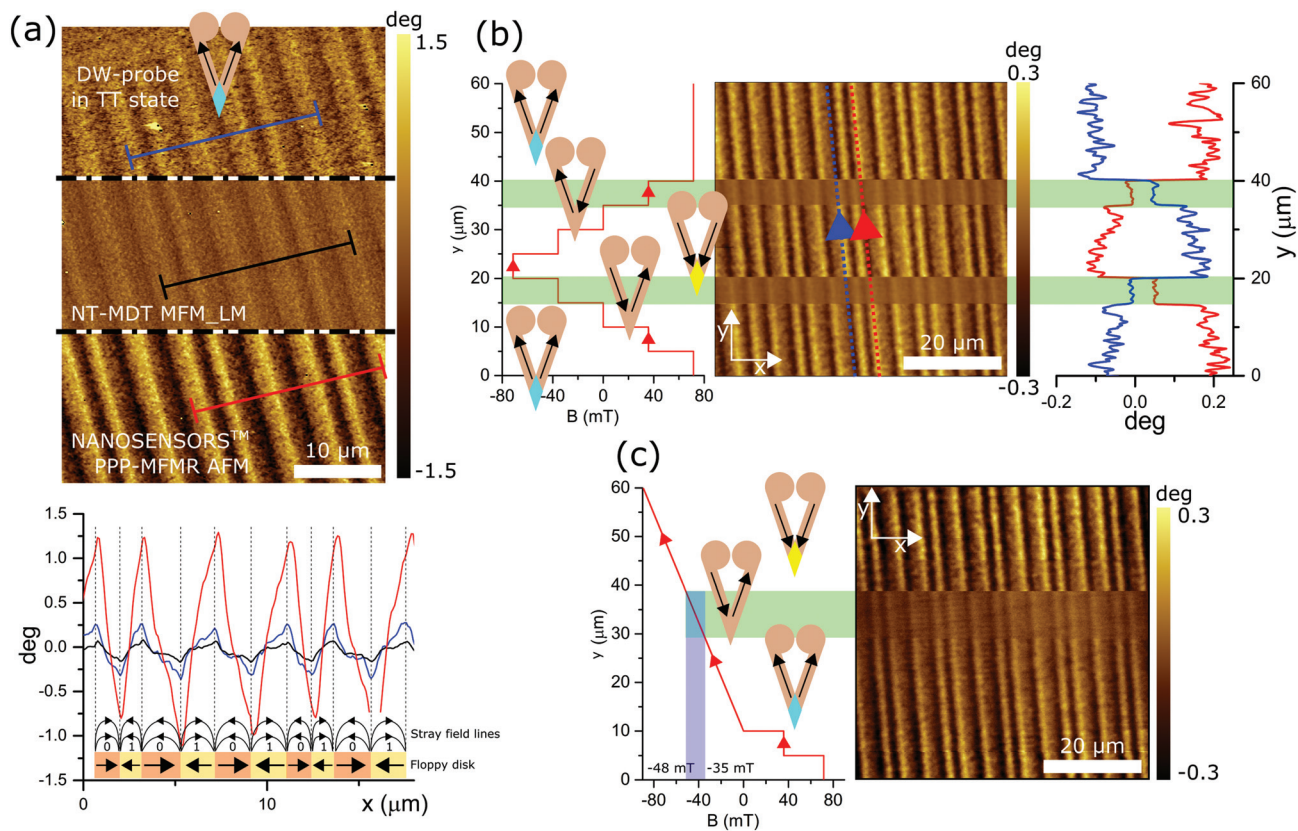
Fig. 4 Variable field MFM of a floppy disk. (a) Top: Comparison between DW-probe in the TT state, the LM probe, and the PPP-MFMR, while performing MFM imaging on the same area of a floppy disk, with the same lift height (40 nm), oscillation amplitude (14 nm), and scan frequency (0.8 Hz). Bottom: Averaged profiles from the top images along with a schematic representation of the floppy disk magnetization and stray field. (b) and (c) In situ MFM images taken with a DW-probe in different applied fields. The field along the z-axis changes (b) in the step-wise manner to demonstrate different states of the probe and (c) gradually during the scan enabling to extract the probe switching fields. Schematics of the probe states and field evolution are shown on the left hand side in (b) and (c). In all the images, the scan direction y is from bottom to top.

consistently with the nucleation of the curl state in the probe. When the field reaches −70 mT (20 μm < y < 25 μm), the DW state is opposite to the initial state (i.e. it is now the HH state). This is convincingly confirmed by the switch of the image magnetic contrast as a result of the flip of the DW polarity, see also the plots of the phase signal along the dotted lines marked in Fig. 4(b). For the rest of the scan (25 μm < y < 60 μm) the external magnetic field is ramped back up from −70 mT to −40, 0, 40, and 70 mT. This time, the DW-probe is in the HH state at 0 mT (30 μm < y < 35 μm) and the signal is the opposite of the one observed at B = 0 during the ramping down of the field (10 μm < y < 15 μm). When the applied magnetic field reaches 40 mT (35 μm < y < 40 μm), the probe is switched into the curl state, producing an MFM signal of much smaller amplitude [Fig. 4(b)] (note that the two curl states observed here have different chirality and thus one shows a magnetic contrast similar to the TT state while the other shows a magnetic contrast similar to the HH state). When the probe reaches the top of the scan in Fig. 4(b), the applied magnetic field is B = 70 mT, and the state of the probe is the same as it was at the beginning (i.e. a TT state) as seen by restoring the bit contrast back to the initial level in Fig. 4(b).

In order to identify the DW-probe switching fields more precisely, an in situ MFM image was taken. First, the probe was saturated with B = 70 mT at the beginning of the scan, then the field was reduced to 40 and 0 mT in a step-wise manner, Fig. 4(c). When the probe is scanning between 10 < y < 60 μm, the field is ramped from zero to negative field values continuously. The MFM contrast in the right-side of Fig. 4(c) shows that the probe transforms into the curl state at −35 mT and eventually switches into HH state at −48 mT. By repeating the cycle several times, (see Fig. S3 in the ESI† for an MFM image with the field ramping up), we can estimate the field required to change a TT or HH state into a curl state being ∼40 mT and that for changing a curl state to a TT or HH ∼50 mT. This demonstrates that the DW-probe possesses a large coercivity bestowed by the geometrical confinement, i.e., shape anisotropy, which implies a strong stability of the magnetization at the V apex corner against local perturbations, including the stray field generated by the sample (it is estimated to be ≪1 mT at the probe-sample distance used in the measurement[35,45,46]). Equally relevant is the fact that the shape anisotropy and the resulting coercivity of the magnetic nanostructure to external (homogeneous) magnetic fields are easily

tuneable by changing the geometrical parameters (width, thickness and length of the arms; the presence/absence of terminating disks, their shape and/or size), without the need to change magnetic material.[40,47,48]

Combining the previously shown EH results with the measurements of the coercive field, the following protocol, using the external magnetic field B, to switch between the different magnetization states of the DW-probe has been stablished:

Apply $B > 50$ mT to obtain a TT state; the probe will be stable to perform in field MFM in the range -40 mT $< B$.

Apply $B < -50$ mT to obtain a HH state; the probe will be stable to perform in field MFM in the range $B < 40$ mT.

First apply $B > 50$ mT to obtain a TT state; then a field in the range -50 mT $< B < -40$ mT to obtain a curl state. The probe will be able to perform in field MFM in the range -50 mT $< B < 40$ mT.

First apply $B < -50$ mT to obtain a HH state; then a field in the range 40 mT $< B < 50$ mT to obtain a curl state. The probe will be able to perform in field MFM in the range -40 mT $< B < 50$ mT.

This protocol allows setting the DW-probes in a certain state prior to the study of samples at remanence or in field, taking into account that the in field studies might be limited depending both on the switching field of the sample and the probe (tuneable by modifying the V-shaped nanostructure).
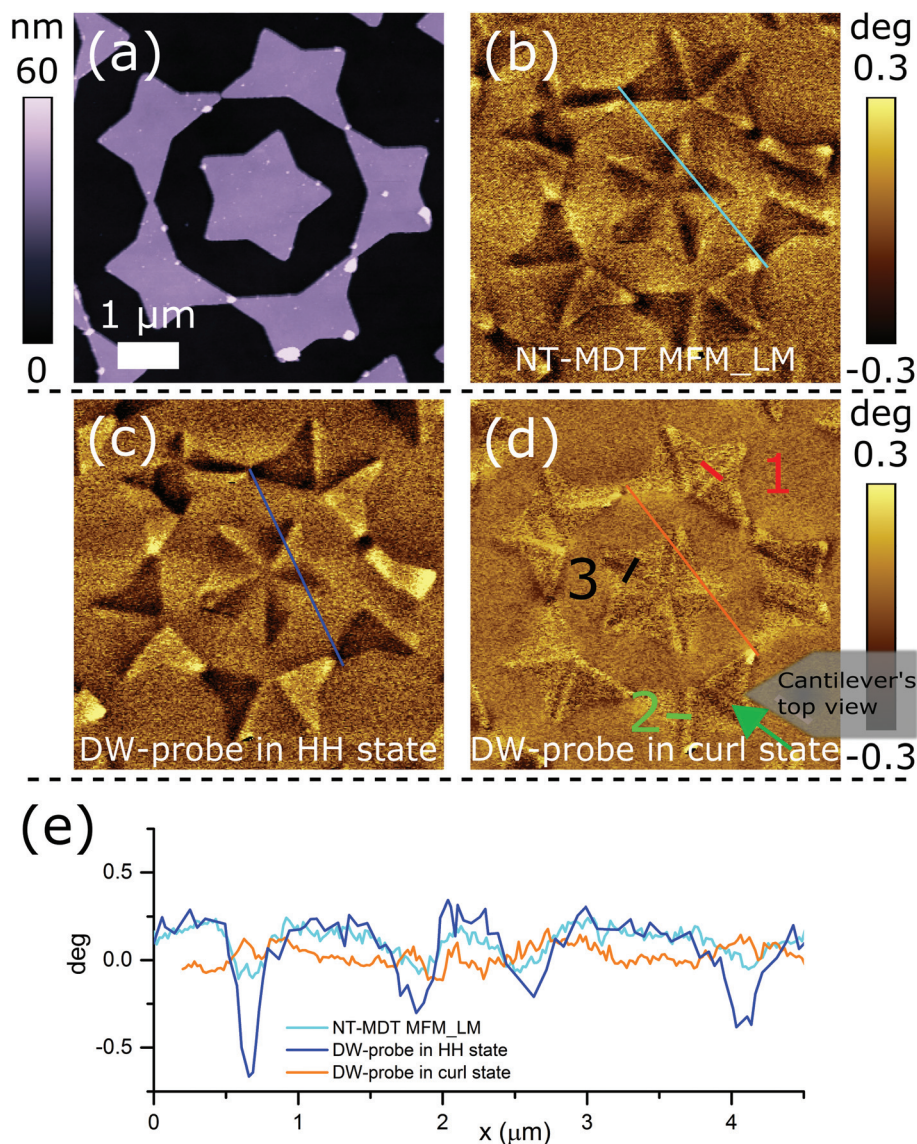

Fig. 5 Comparison of MFM probes when imaging a complex sample. (a) Topography of a small area of a Penrose pattern. MFM image taken using (b) the low moment NT-MDT MFM_LM probe; the DW-probe in (c) HH and (d) curl states. Inset: Orientation of the probe during scanning with green arrow indicating the direction of the stray field at the apex. (e) Cross sections taken from turquois, blue, and orange lines in (b)−(d) respectively. Red, green and black lines numbered 1, 2, 3 in (d) mark the position of cross-sections analyzed in Fig. 6.

To further evaluate the performance of different probes, a patterned magnetic nanostructure made of Py (25 nm thick) was imaged using MFM (Fig. 5). The chosen nanostructure is part of a Penrose pattern used for e-beam alignment in nanofabrication.[49,50] This pattern forms a complex domain structure localized in a small area, enabling comparison of different probes against a particularly complex and challenging case. An approach to compare probes through the real-space probe transfer function and quantitative MFM was recently presented for a similar concept of DW-probes, however, with a different V-shaped design.[51]

Topography and MFM images of the Penrose pattern recorded with a commercial low moment NT-MDT MFM_LM probe are shown in Fig. 5(a) and (b), respectively. After taking these images, the probe was replaced with the DW-probe and the next set of images shown in Fig. 5(c) and (d) was taken with the probe in HH and curl states, respectively [notice that some mismatch between the topography and magnetic apexes will appear here in the form of a superimposition of the MFM and topography images only if it is larger than the MFM resolution, but since this type of artefact is not seen in either Fig. 5(c) or (d), it is possible to conclude that it's effect is

smaller than the MFM resolution for both HH and curl states]. Profiles of Fig. 5(b)–(d) shown in Fig. 5(e) demonstrate that the change in the amplitude is two times larger for the DW-probe (~0.6 deg in the HH state) as compared to low moment probe (~0.3 deg). Reducing down to ~0.25 deg in the curl state. This confirms that the DW-probe in the HH/curl state is characterized by larger/smaller magnetic moments with respect to the commercial probe. Furthermore, the side to side comparison using the profiles, shown in Fig. 5(e), demonstrates that the image recorded with the DW-probe has a higher resolution than that taken with the commercial low moment one, in spite of the similar magnetic contrast (applying the 20–80% Edge Spread Function defined in Standards on Lateral Resolution[52]). The improved resolution of the DW-probe arises from the much higher localization of the magnetic stray field source in the geometrically constrained DW. At the same time, when comparing Fig. 5(b)–(d), we conclude that the DW-probe interference with sample magnetization is negligible, similar to the commercial low moment probe. This is further supported by the match between Fig. 5(b)–(d) with the expected magnetic configuration as calculated by micromagnetic simulations, and by the imaging artefacts created by a probe that
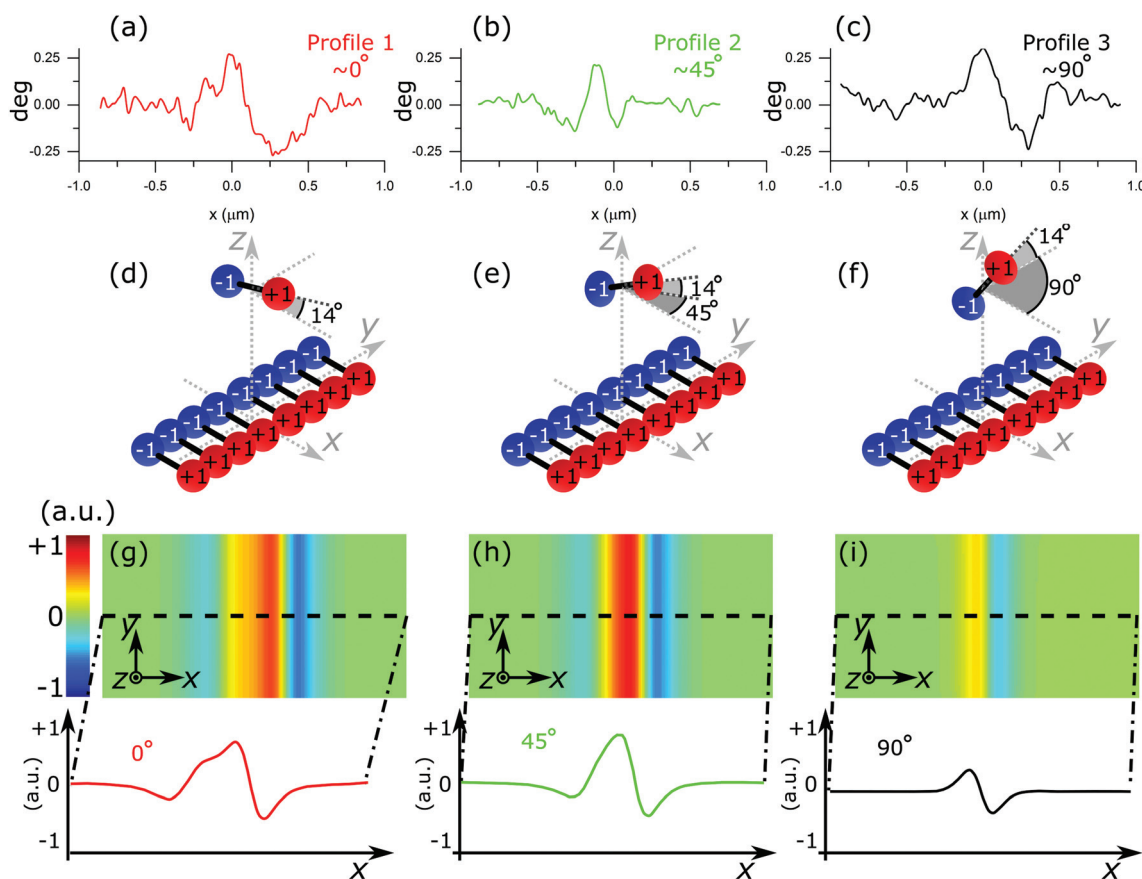

Fig. 6 Simulated dipole response. Top: MFM phase signal profiles extracted from Fig. 5(f). Middle: Schematic representation of the probe dipole and the surface chain of dipoles. Bottom: Calculated $\frac{\partial F_z}{\partial z}$ maps when the dipole representing the probe scans over the chain of dipoles representing the DW. Red, green and black curves in (g), (h) and (i) represent cross sections of the maps shown in (a), (b), and (c) respectively. In all cases, the DW-probe moment is in plane of the sample; the mutual orientation of the probe dipole and the DW are parallel (g); at 45° (h) and perpendicular (i).

interacts strongly with the sample's magnetization, see Fig. S4 and S5 in the ESI.†

Further inspection of Fig. 5(b–d) reveals that for all probes characterized by strong stray field (*i.e.* NT-MDT MFM_LM and DW-probe in HH state) the interaction between domain boundaries in the sample and the probe is a mono-pole like and sensitive to the divergence of the magnetization, *i.e.* $\nabla(M)$, thus creating a dark-bright sharp transition when the probe scans over a boundary between adjacent domains. This corroborates a distinction between different types of such boundaries, that could occur in samples depending on local anisotropy, exchange interaction, geometrical constraints *etc.*, is generally not achievable with conventional MFM.[53] In this respect, it is remarkable that a closer inspection of Fig. 5(d) shows that the magnetic contrast obtained with the DW-probe in the curl state is qualitatively different from the others since it highlights the boundaries in between domains rather than the domains themselves. In Fig. 6(a)–(c) we further analyze boundary cross sections of Fig. 5(d), see *e.g.* red, green and black lines. The phase profiles depend on the orientation between the magnetic dipole associated to the DW-probe in the curl state and the domain boundary. This utmost property of our DW-probe in the curl state leads to a sensitivity of the DW-probe in the curl state to the rate of the divergence change, *i.e.* $\nabla^2(M)$. This can be appropriately modeled using a simple magnetic dipolar model described in detail in the Experimental section. Fig. 6(d), (e), and (f) show a schematic of the model, where the probe is represented by a magnetic dipole and the domain boundary by a chain of dipoles representing the charge accumulation created by the DWs in the Penrose pattern. Fig. 6(d) denotes the case of probe's dipole in-plane projection parallel to the dipoles in the chain representing the boundary [corresponding to profile 1 in Fig. 5(d)]. The 45° case is shown in Fig. 6(e) [see also profile 2 in Fig. 5(d)] and the 90° case – in Fig. 6(f). The 14° angle was introduced to take into account the tilting created by the probe holder. This simple model allows the calculation of the force gradient maps and line plots in Fig. 6(g)–(i). The maps show the force gradient along the *z*-axis $\left(\dfrac{\partial F_z}{\partial z}\right)$, when the magnetic dipole of the probe scans over the chain of dipoles describing the boundary. Both the maps and the map profiles taken along the dashed lines demonstrate that the signal measured by the DW-probe in the curl state depends on the relative orientation of the probe and the boundary (whereas the scanning direction is not important). The comparison between the experimental profiles, Fig. 6(a)–(c), and the simulated ones, *i.e.* bottom panels of Fig. 6(g)–(i), shows an excellent agreement that demonstrates that the DW-probe allows differentiating different types of boundaries in between domains, thereby enabling studies of DWs in planar structures with unprecedented resolution. Moreover, by combining images obtained in the HH/TT states with those taken with the curl state, it is possible to extract 3D information about the sample's magnetization, and hence the DW-probe allows for detailed studies of 3D distribution of magnetization on nanoscale.

Conclusions

We demonstrate a new concept of MFM probes exploiting the peculiar magnetic properties of V-shaped magnetic nanostructures. Such new probes are obtained by FIB-milling of commercial pyramidal MFM probes to leave a V-shaped magnetic nanostructure on one of the sides of the pyramid. This magnetic nanostructure possesses four stable magnetic states, two with a nanometer-size geometrically constrained DW at the corner of the V-shape, and two states without a DW in which magnetization is curling along the corner. An external magnetic field of moderate intensity allows for selecting the desired magnetic state in the probe. EH results and numerical simulations demonstrate that the two DW states (*i.e.* HH and TT states) generate a strong stray field with opposite polarity in the direction of the probe axis (monopole-like point field sources), while the two states without DW (curl states) produce a much weaker and dipole-like stray field that is perpendicular to the previous one.

In situ MFM imaging demonstrated that the phase contrast achieved with the DW-probe in the TT or HH state is twice as large as that from a commercial low moment probe, simultaneously demonstrating improved spatial resolution in respect to the low moment probe, which arises from the nanometer localization of the magnetic stray field source, *i.e.*, the geometrically constrained DW at the V-shaped nanostructure apex. We also demonstrated that we can controllably set the magnetization of the DW-probe using an externally applied magnetic field, thus enabling different magnetic imaging modes. The large coercivity of the probe, due to the strong shape anisotropy of the V-shaped structure, insures the stability of magnetic configurations of the DW-probe that in combination with the low magnetic moment guarantees a negligible interference with the magnetic state of the sample. Using a Penrose pattern as a complex and particular challenging test magnetic nanostructure, it was shown that the DW probe is able to achieve better spatial and magnetic resolution and higher magnetic resolution with respect to commercial probes of similar magnetic moment. In addition, the DW-probe in curl state is selectively sensitive to the boundaries in between domains, enabling the determination of their internal magnetic structure with unprecedented resolution.

Thus, the DW-probe concept meets the requirements of advanced MFM: it combines high sensitivity and spatial resolution with high probe stability and low stray field; it gives the possibility to adapt probe characteristics to the local sample properties for samples with highly heterogeneous physical properties; it has sensitivity to fine details of the 3D magnetization distribution at the nanoscale. Moreover, the special characteristics of the DW-probe can potentially be used in new MFM imaging modes, *e.g.* by exploiting stable low and high moment states, it is possible to use these probes in differential phase imaging (switching DW polarity in a double pass approach) or controlled magnetization MFM[35] (four pass approach using the four magnetization states to fully cancel electrostatic interactions). Also, the possibility to set the DW

probe in a low moment curl state could, in principle, allow for recording a "true" sample topography by switching off magnetic interactions (setting the probe to a curl state) in the first pass, before probing the magnetic contrast by scanning over the surface at constant height from (setting the tip to a DW state). This is advantageous over the conventional magnetic probes, where magnetic interactions are active even during the first topography pass, thus always leading to intermixing of topographic and magnetic signals that limits the quantitative use of MFM.[54]

Experimental section

The modified probes were custom-made using magnetically coated commercial probes from NANOSENSORS™ PPP-MFMR AFM[43] and focused ion beam (FIB) to etch away part of the magnetic coating. As it can be seen in Fig. 1(a)–(c), the probe of these probes has 4 triangular sides which are uniformly coated with a CoCr alloy. Dimensions of the probe's side, when approximated by a triangle, are 8.15 μm in height by 4.73 μm length of the base [Fig. 1(c)]. FIB milling lithography (Ga-ions) is used to etch away the magnetic material from the probe's sides: completely from three sides, while leaving only a V-shaped magnetic nanostructure on one of them [Fig. 1(d)]. The V-shaped nanostructure's arms are 4.48 μm in length by 200 nm in width, and they meet at 32.3°. The estimated thickness[17] of the magnetic coating is about 30 nm. Both arms of the V-shaped nanostructure are terminated by a circular disc of 1 μm in diameter to reduce the stray field produced by the end parts of the nanostructure and reduce the coercive field required to reverse magnetization.[40,47,48] Although the exact composition of the magnetic coating of the commercial probes from NANOSENSORS™ PPP-MFMR AFM is unknown, it is expected that it possess in-plane magnetization, and hence the V-shaped structure is expected to behave similarly to ferromagnetic structures of similar dimensions with in-plane magnetization (e.g. 25 nm thick Py L-shaped nanostructures[40,41]), which shows four stable magnetic states depending on the magnetization along the arms.

Micromagnetic numerical simulations were carried out using OOMMF micromagnetic solver from NIST.[55] As shape anisotropy is expected to dominate over magnetocrystalline anisotropy, the cell size used was $5 \times 5 \times 5$ nm^3, and the material parameters used were the standard for Py ($M_s = 800 \times 10^3$ A m^{-1}, $A = 13 \times 10^{-12}$ J m^{-1}, $k = 0$). Magnetic charge density maps were calculated using $\rho_{Vol} = -\vec{\nabla}\vec{M}$.

The SPM system (Aura from NT-MDT with custom made magnet for applying out-of-plane fields) was used for *in situ* MFM studies in ambient atmosphere and at room temperature.

EH imaging[56] of the stray magnetic field produced by the modified probes was carried out in a Hitachi HF3300 (I2TEM-Toulouse) microscope, a transmission electron microscope (TEM) specially designed to perform *in situ* EH experiments with a high resolution and phase shift sensitivity

thanks to a very high brightness cold field emission gun and a spherical aberration corrector (aplanator B-COR from CEOS) to correct the off-axial aberration in both TEM and Lorentz modes.[56] For this study, EH experiments were performed in a corrected Lorentz mode for the normal stage of the microscope. In this stage the sample is placed within the pole pieces of the objective lens which is switched off to favor a free-field condition. However, a controlled magnetic field can be applied by exciting the objective lens, which acts parallel to the electron trajectory. This *in situ* magnetic field capability of the microscope was used to change the magnetic states of the MFM probes. EH holograms were recorded operating the microscope at 300 kV, and using a double bi-prism setup to avoid the formation of Fresnel fringes in the lateral edges of the hologram. The reconstruction of the stray field around the probe was carried out by retrieving, from the holograms, the magnetic component of the phase shift of the object electron wave, $\varphi_{MAG}(z, y)$, which is directly proportional to the magnetic flux,[56] $\Phi(z, y)$, $[\varphi_{MAG}(z, y) = (e/\hbar)\Phi(z, y)$, where e and $\hbar$ are the electron charge and the reduced Planck constant, respectively] so images of the phase shift will directly provide maps of the magnetic flux. In addition, $\varphi_{MAG}(z, y)$ and the projected magnetic induction, $B_{proj}(z, y)$ are related as[57] $\nabla\varphi_{MAG}(z, y) \cdot B_{proj}(z, y) = 0$, meaning that the variation of the magnetic phase shift is perpendicular to the direction of the projected magnetic induction, following the right-hand rule between $\nabla\varphi_{MAG}(z, y)$, $B_{proj}(z, y)$ and the electron trajectory. This relationship allow us determining the direction of the magnetic flux.

In order to identify all the stable magnetization states when performing EH, the DW-probe, which is placed inside of the TEM with the pyramid along the $+z$-axis to perform EH [schematically represented in Fig. 2(g)], is rotated to place the pyramid along the $+x$-axis, and then a strong saturation field is applied towards $-x$-axis [Fig. 2(g)]. According to the probe position inside the TEM, such condition should induce a TT DW. At zero-field condition, the DW probe is tilted back with the pyramid apex pointing in the direction of the $+z$ and $-x$-axes [*i.e.* at 45° in respect to both x and z-axes as depicted in Fig. 2(g)]. In such configuration, the applied magnetic field was progressively increased until each representative magnetic state was obtained. However, whenever a change in the magnetization was detected, the magnetic field was reduced to zero and the probe was tilted with the apex pointing towards $+z$-axis in order to image the state at remanence.

To facilitate the interpretation of the stray field configuration, magnetic flux line representation [Fig. 2(d–f)] was produced by applying a sinusoidal function to the amplified magnetic phase shift images [Fig. 2(a–c)], *i.e.* $\Phi(y, z) \sim \cos(n\varphi_{MAG}(y, z))$, where $\Phi(y, z)$ is the magnetic flux representation, n is an enhancement factor, and $\varphi_{MAG}(y, z)$ is the electron beam phase shift.

Simulations of dipolar interaction between the DW-probe in the curl state (approximated as a dipole) and the DWs in the Penrose pattern (approximated as a line of dipoles) were carried out using a simplistic magnetic dipolar model. The curl state was approximated by two magnetic charges $q_1^{probe} =$

+1 and $q_2^{\text{probe}} = -1$ separated by 1 a.u., and aligned along x-axis or y-axis [as shown in Fig. 6(d) and (e) respectively]. A small tilt of 14° was introduced to take into account the tilting created by the probe holder. The DWs in the Penrose pattern were approximated by 200 + 1 and −1 surface charges along the y-axis as illustrated in Fig. 6(d) and (e). Each pair of charges is separated by 0.00125 a.u. and the 200 pairs span along 10 a.u. along the y-axis. The dipole representing the probe is supposed to scan at a light height of 1.125 a.u. The force used in the dummy magnetic dipolar model was:

$$\vec{F} = \sum_{i=1}^{2}\sum_{j=1}^{200}\frac{q_i^{\text{probe}} q_j^{\text{sample}}}{r_{ij}^2}\hat{r}_{ij} \tag{1}$$

Conflicts of interest

There are no conflicts to declare.

Acknowledgements

Notes and references

1 R. Nagatsu, M. Ohtake, M. Futamoto, F. Kirino and N. Inaba, *AIP Adv.*, 2016, **6**, 056503.
2 J. Heo, K. Kim, T. Kim and I. Chung, in *2006 IEEE Nanotechnology Materials and Devices Conference*, IEEE, 2006, vol. **2667**, pp. 618–619.
3 E. D. Cobas, O. M. J. van 't Erve, S.-F. Cheng, J. C. Culbertson, G. G. Jernigan, K. Bussman and B. T. Jonker, *ACS Nano*, 2016, **10**, 10357–10365.
4 Y. Wang, H. Yu, L. Ni, G.-B. Huang, M. Yan, C. Weng, W. Yang and J. Zhao, *IEEE Trans. Nanotechnol.*, 2015, 1–1.
5 Y. P. Ivanov, A. Alfadhel, M. Alnassar, J. E. Perez, M. Vazquez, A. Chuvilin and J. Kosel, *Sci. Rep.*, 2016, **6**, 24189.
6 E. Rapoport and G. S. D. Beach, *Sci. Rep.*, 2017, **7**, 10139.
7 S. N. Piramanayagam, M. Ranjbar, R. Sbiaa, A. Tavakkoli K. G. and T. C. Chong, *Phys. Status Solidi RRL*, 2012, **6**, 141–143.
8 J. M. García-Martín, A. Thiaville, J. Miltat, T. Okuno, L. Vila and L. Piraux, *J. Phys. D: Appl. Phys.*, 2004, **37**, 965–972.
9 O. Iglesias-Freire, J. R. Bates, Y. Miyahara, A. Asenjo and P. H. Grütter, *Appl. Phys. Lett.*, 2013, **102**, 022417.
10 M. R. Koblischka, U. Hartmann and T. Sulzbach, in *Thin Solid Films*, 2003, vol. 428, pp. 93–97.
11 H. Corte-León, B. Gribkov, P. Krzysteczko, F. Marchi, J.-F. Motte, H. W. Schumacher, V. Antonov and O. Kazakova, *J. Magn. Magn. Mater.*, 2016, **400**, 225–229.
12 N. Amos, A. Lavrenov, R. Fernandez, R. Ikkawi, D. Litvinov and S. Khizroev, *J. Appl. Phys.*, 2009, **105**, 07D526.
13 I. Utke, P. Hoffmann, R. Berger and L. Scandella, *Appl. Phys. Lett.*, 2002, **80**, 4792.
14 D. Litvinov and S. Khizroev, *Appl. Phys. Lett.*, 2002, **81**, 1878.
15 H. Campanella, M. Jaafar, J. Llobet, J. Esteve, M. Vázquez, A. Asenjo, R. P. del Real and J. a. Plaza, *Nanotechnology*, 2011, **22**, 505301.
16 Y. Lisunova, J. Heidler, I. Levkivskyi, I. Gaponenko, A. Weber, C. Caillier, L. J. Heyderman, M. Kläui and P. Paruch, *Nanotechnology*, 2013, **24**, 105705.
17 M. Jaafar, A. Asenjo and M. Vázquez, *IEEE Trans. Nanotechnol.*, 2008, **7**, 245–250.
18 A. Thiaville, L. Belliard, D. Majer, E. Zeldov and J. Miltat, *J. Appl. Phys.*, 1997, **82**, 3182.
19 Ó. Iglesias-Freire, M. Jaafar, E. Berganza and A. Asenjo, *Beilstein J. Nanotechnol.*, 2016, **7**, 1068–1074.
20 H. Campanella, R. P. Del Real, M. Díaz-Michelena, M. Duch, H. Guerrero, J. Esteve and J. a. Plaza, *ACS Appl. Mater. Interfaces*, 2009, **1**, 527–531.
21 D. Sander, S. O. Valenzuela, D. Makarov, C. H. Marrows, E. E. Fullerton, P. Fischer, J. McCord, P. Vavassori, S. Mangin, P. Pirro, B. Hillebrands, A. D. Kent, T. Jungwirth, O. Gutfleisch, C. G. Kim and A. Berger, *J. Phys. D: Appl. Phys.*, 2017, **50**, 363001.
22 J. García a Thiaville and J. Miltat, *J. Magn. Magn. Mater.*, 2002, **249**, 163–169.
23 A. Alekseev, A. Popkov, A. Shubin, F. Pudonin and N. Djuzhev, *Ultramicroscopy*, 2014, **136**, 91–95.
24 T. Uhlig, U. Wiedwald, A. Seidenstücker, P. Ziemann and L. M. Eng, *Nanotechnology*, 2014, **25**, 255501.
25 F. Wolny, Y. Obukhov, T. Mühl, U. Weissker, S. Philippi, A. Leonhardt, P. Banerjee, A. Reed, G. Xiang, R. Adur, I. Lee, a. J. Hauser, F. Y. Yang, D. V. Pelekhov and P. C. Hammel, *Ultramicroscopy*, 2011, **111**, 1360–1365.
26 S. Vock, F. Wolny, T. Mühl, R. Kaltofen, L. Schultz, B. Büchner, C. Hassel, J. Lindner and V. Neu, *Appl. Phys. Lett.*, 2010, **97**, 252505.

27 F. Wolny, T. Mühl, U. Weissker, K. Lipert, J. Schumann, A. Leonhardt and B. Büchner, *Nanotechnology*, 2010, **21**, 435501.

28 N. Yoshida, M. Yasutake, T. Arie, S. Akita and Y. Nakayama, *Jpn. J. Appl. Phys.*, 2002, **41**, 5013–5016.

29 F. Wolny, T. Mühl, U. Weissker, A. Leonhardt, U. Wolff, D. Givord and B. Büchner, *J. Appl. Phys.*, 2010, **108**, 013908.

30 T. Arie, N. Yoshida, S. Akita and Y. Nakayama, *J. Phys. D: Appl. Phys.*, 2001, **34**, L43–L45.

31 N. Amos, R. Ikkawi, R. Haddon, D. Litvinov and S. Khizroev, *Appl. Phys. Lett.*, 2008, **93**, 203116.

32 Y. Shen and Y. Wu, *IEEE Trans. Magn.*, 2004, **40**, 97–100.

33 V. Panchal, H. Corte-León, B. Gribkov, L. A. Rodriguez, E. Snoeck, A. Manzin, E. Simonetto, S. Vock, V. Neu and O. Kazakova, *Sci. Rep.*, 2017, **7**, 7224.

34 V. Cambel, D. Gregušová, P. Eliáš, J. Fedor, I. Kostič, J. Maňka and P. Ballo, *J. Electr. Eng.*, 2011, **62**, 37–43.

35 L. Angeloni, D. Passeri, M. Reggente, D. Mantovani and M. Rossi, *Sci. Rep.*, 2016, **6**, 26293.

36 J. Schwenk, M. Marioni, S. Romer, N. R. Joshi and H. J. Hug, *Appl. Phys. Lett.*, 2014, **104**, 112412.

37 B. I. Kim, *J. Appl. Phys.*, 2012, **111**, 104313.

38 M. Precner, J. Fedor, J. Šoltýs and V. Cambel, *Nanotechnology*, 2015, **26**, 055304.

39 P. Vavassori, M. Gobbi, M. Donolato, M. Cantoni, R. Bertacco, V. Metlushko and B. Ilic, *J. Appl. Phys.*, 2010, **107**, 09B301.

40 M. Donolato, M. Gobbi, P. Vavassori, M. Leone, M. Cantoni, V. Metlushko, B. Ilic, M. Zhang, S. X. Wang and R. Bertacco, *Nanotechnology*, 2009, **20**, 385501.

41 H. Corte-León, V. Nabaei, A. Manzin, J. Fletcher, P. Krzysteczko, H. W. Schumacher and O. Kazakova, *Sci. Rep.*, 2014, **4**, 6045.

42 S. Signoretti, C. Beeli and S.-H. Liou, *J. Magn. Magn. Mater.*, 2004, **272–276**, 2167–2168.

43 NANOSENSORSTM Magnetic Force Microscopy Silicon-MFM-Probes, http://www.nanosensors.com/downloads, 2016.

44 MFM_LM, http://ntmdt-Tips.com/products/view/mfm-Lm, 2017.

45 D. Passeri, C. Dong, L. Angeloni, F. Pantanella, T. Natalizi, F. Berlutti, C. Marianecci, F. Ciccarello and M. Rossi, *Ultramicroscopy*, 2014, **136**, 96–106.

46 I. G. Hughes, P. A. Barton, T. M. Roach and E. A. Hinds, *J. Phys. B: At., Mol. Opt. Phys.*, 1997, **30**, 2119–2132.

47 A. Manzin, V. Nabaei, H. Corte-León, O. Kazakova, P. Krzysteczko, H. W. Schumacher, H. Corte-Leon, O. Kazakova, P. Krzysteczko and H. W. Schumacher, *IEEE Trans. Magn.*, 2014, **50**, 1–4.

48 H. Corte-Leon, A. Beguivin, P. Krzysteczko, H. W. Schumacher, A. Manzin, R. P. Cowburn, V. Antonov and O. Kazakova, *IEEE Trans. Magn.*, 2015, **51**, 1–4.

49 K. E. Docherty, K. A. Lister, J. Romijn and J. M. R. Weaver, *Microelectron. Eng.*, 2009, **86**, 532–534.

50 K. E. Docherty, S. Thoms, P. Dobson and J. M. R. Weaver, *Microelectron. Eng.*, 2008, **85**, 761–763.

51 R. Puttock, H. Corte-Leon, V. Neu, D. Cox, A. Manzin, V. Antonov, P. Vavassori and O. Kazakova, *IEEE Trans. Magn.*, 2017, **53**, 1–5.

52 M. Senoner and W. E. S. Unger, *Surf. Interface Anal.*, 2013, **45**, 1313–1316.

53 C. Rawlings and C. Durkan, *Nanotechnology*, 2013, **24**, 305705.

54 H. J. Hug, B. Stiefel, P. J. a. van Schendel, a. Moser, R. Hofer, S. Martin, H.-J. Güntherodt, S. Porthun, L. Abelmann, J. C. Lodder, G. Bochi and R. C. O'Handley, *J. Appl. Phys.*, 1998, **83**, 5609.

55 M. J. Donahue and D. G. Porter, *OOMMF User's Guide, Version 1.0. Interagency Report NISTIR 6373*, Gaithersburg, 1999.

56 D. Shindo and Y. Murakami, *J. Phys. D: Appl. Phys.*, 2008, **41**, 183002.

57 H. Lichte and M. Lehmann, *Rep. Prog. Phys.*, 2008, **71**, 016102.